NJC

Accepted Manuscript

This is an *Accepted Manuscript*, which has been through the Royal Society of Chemistry peer review process and has been accepted for publication.

Accepted Manuscripts are published online shortly after acceptance, before technical editing, formatting and proof reading. Using this free service, authors can make their results available to the community, in citable form, before we publish the edited article. We will replace this *Accepted Manuscript* with the edited and formatted *Advance Article* as soon as it is available.

You can find more information about *Accepted Manuscripts* in the Information for Authors.

Please note that technical editing may introduce minor changes to the text and/or graphics, which may alter content. The journal's standard Terms & Conditions and the Ethical guidelines still apply. In no event shall the Royal Society of Chemistry be held responsible for any errors or omissions in this *Accepted Manuscript* or any consequences arising from the use of any information it contains.

ROYAL SOCIETY OF CHEMISTRY

www.rsc.org/njc

Design of New Magnetic-Photocatalyst Nanocomposites ($CoFe_2O_4$-TiO_2) as Smart Nanomaterials for Recyclable-Photocatalysis Application

Choonyian Haw,[a] Weesiong Chiu,[a*] Saadah Abdul Rahman,[a] Poisim Khiew,[b] Shahidan Radiman,[c] Roslan Abdul Shukor,[c] Muhammad Azmi Abdul Hamid,[c] and Naziri Ghazali[d]

[a]Low Dimensional Materials Research Centre, Department of Physics, University of Malaya, 50603 Kuala Lumpur, Malaysia.

[b]Department of Chemical Engineering, Faculty of Engineering, University of Nottingham Malaysia Campus, Jalan Broga, 43500 Semenyih, Selangor Darul Ehsan, Malaysia.

[c]School of Applied Physics, Faculty of Science and Technology, Universiti Kebangsaan Malaysia, 43600 UKM Bangi, Selangor Darul Ehsan, Malaysia.

[d]Naz Scientific Sdn. Bhd, No. 14B, ½ Road, Kajang Teknologi Town, Section 1, 43500 Semenyih, Selangor Darul Ehsan, Malaysia.

*Correspondence should be addressed to Wee Siong Chiu; w.s.chiu@um.edu.my

Abstract

Current study reports the synthesis and characterisation of a new magnetic-photocatalyst ($CoFe_2O_4$-TiO_2) and tests its feasibility to be used as smart magnetically-recoverable nanomaterials in photodegradation of methylene blue (MB). The 3D urchin-like TiO_2 microparticles are hydrothermally prepared and decorated with $CoFe_2O_4$ magnetic nanoparticles (NPs) through a co-precipitation method. The as-prepared $CoFe_2O_4$-3D TiO_2 nanocomposites show enhancement in photodegradation of MB if compared to commercial rutile-phase TiO_2 and pure urchin-like TiO_2 (3D TiO_2) microparticles. Such enhancement could be accredited to the lower recombination rate of photoexcited charge carriers of $CoFe_2O_4$-3D TiO_2 nanocomposites. Furthermore, the $CoFe_2O_4$-3D TiO_2 nanocomposite is magnetically-retrievable for sequential recyclability, and the results indicate that the nanocomposite shows a relatively consistent photocatalytic performance with negligible degradation. Thus, the current study would offer a potential route in the design and processing of a value-added photocatalyst nanocomposite that will contribute to the advancement of photocatalysis study.

Keywords: $CoFe_2O_4$-TiO_2 nanocomposite; Magnetic separable photocatalysts; Photocatalytic degradation; Methylene blue; Urchin-like TiO_2

1. Introduction

In searching to develop high efficiency and stable photocatalytic materials to combat global issues such as water crises and wastewater treatment, TiO_2-based photocatalyst appear as an efficient pollution-control technology due to their versatility, controllability and handy operation.[1-4] Generally, photocatalysis converts the incoming photon energy into chemical energy, which requires a material that generates a transient state upon light absorption, producing an electron-hole pair to form some chemical species. This in turn will render the photocatalytic redox reactions cascading from a higher energy state to lower energy state.

One of the prerequisites of a photocatalyst is the stability and durability under constant irradiation in order to sustain its continual reusability for several cycles. However, the major drawback with UV photocatalysis is its limited solar spectrum of 4% compared to (46%) for visible light.[5] Apart from that, many studies revealed that anatase was found to have the greatest photocatalytic activity compared to the other polymorphs of TiO_2. Studies have shown that anatase TiO_2 can transform into rutile phase when the size of the particle exceeds more than 30 nm.[6,7] Also, the photocatalytic materials should have a proper band position ranging from 1.23 eV to 3.0 eV for optimum harnessing of UV spectrum. By taking these effects into account, many researchers are aware for that the stability of a TiO_2 crystal structure, phase transformation and suitable band gap energy play vital roles in facilitating photocatalytic performances such as degradation of organic dyes and pollutants in wastewater treatment.

Majority of research has been carried out on anatase TiO_2, while rutile TiO_2 is less frequently adopted in photocatalysis applications, possibly due to lower direct allowed band gap energy (~3.03 eV) than that of anatase TiO_2 (3.20 eV).[8] Moreover, slow electron mobility is also another drawback of rutile TiO_2 that may lead to higher electron densities within the highest occupied molecular orbital (HOMO); this can increase the quasi Fermi-level and thus render the higher redox potential to further produce the adsorbed chemical species activated by UV irradiation.[9] Indeed, many studies have shown that rutile TiO_2 can achieve similar or even lower band gap energy through doping.[10-12] Furthermore, as compared to the anatase TiO_2, the rutile

polymorph of TiO_2 exhibits other physical properties, such as enhanced light-scattering properties on account of its higher refractive index, which is an advantage from the perspective of effective light harvesting.[13] Moreover, rutile TiO_2 has been proven to have better electrical conductivity than other polymorphs of TiO_2. This is ascribed to the larger electron effective mass of rutile, which can increase the carrier density directly and causes the resistance of the rutile to be lower than that of anatase.[14] Additionally, rutile TiO_2 is the most thermodynamically stable and dense state phase of TiO_2.[15] In addition, the efficiency of TiO_2 as photocatalytic material also depends strongly on some crucial factors such as particle size, stoichiometric composition, surface modification, hydrophilicity and morphological structures.[16,17] Most importantly, a better performance of TiO_2 requires high specific surface area-to-volume ratio enabling the optimum hydrophilicity of adsorbed molecules such as concomitant organic dye molecules that dissolve in a water environment. In general, rutile phase TiO_2 tends to form in the elongated rod-like structure with a high aspect ratio of length to width. The feasibility for this 1D rod-like structure can be further self-assembled into a 3D urchin-like microstructure with a very high surface area. Such a high surface area together with its congruent electronic properties that promote the efficient charge separation indeed can contribute significantly towards the overall photocatalysis performance. For instance, in the case of photodegradation of organic-dye compounds, this is important in order to increase the passivation of the dissolved organic dye molecules to the active sites of the photocatalyst surface while being able to absorb large quanta of photons.

In the light of the above facts, synthesizing of a stable, highly crystalline and well-defined hierarchical three-dimensional (3D) TiO_2 nanostructures has become a vital task in the present work. This work was inspired by the work of Xiang et al. (2012), who successfully prepared three dimensional hierarchical (3D) urchin-like TiO_2 nanostructures, which were proved to be a promising photocatalyst material in photocatalytic degradation of organic dye molecules for wastewater treatment.[18] Tian et al. (2011) have successfully synthesis 3D hierarchical flower-like TiO_2 nanostructure that exhibit better photocatalytic performance as compared to that of Degussa P25 for the degradation of phenol under UV radiation.[19] Meanwhile, Jiang et al. (2014) have also successfully produced 3D structure of TiO_2 spheres and evaluate its feasibility in degradation of methyl orange dye.[20] All of these studies have indicated that by

tailoring a TiO_2 nanostructure from a 0D to 3D hierarchical structure will possibly offer an highly potential route to manipuluate and further leverage the properties of TiO_2, especially for photocatalytic applications in wastewater treatment.

Despite numerous of efforts have been dedicated in improving the photocatalytic performance for TiO_2, however, the suspension-based photocatalysis process remains bear heavily to be practised in real life due to the difficulty in separation of the photocatalyst from the treated-water as well as its feasibility to be reused for sequencial cycles. All these factors will ultimately render excessive cost for such photocatalysis technology to be practised with major concern on the economic perception. Therefore, there is a dire need to integrate a novel separation feature into TiO_2 photocatalyst materials. Lately, magnetic separation have been found to offer a very convenient avenue for removing and recycling magnetic particles/composites by applying the external magnetic field.[21,22] This approach can prevent the sedimentation and agglomeration of the photocatalyst particles during the recovery stage, and thus can increase the durability of the photocatalyst in the subsequent treatment process.

As complementary efforts to previous studies[18-22], current study reports the synthesis of a new magnetic-photocatalyst ($CoFe_2O_4$-TiO_2) and evaluates its photocatalytic performance as a smart magnetically-recoverable nanomaterial in photodegradation of MB. The 3D urchin-like TiO_2 microparticles were hydrothermally synthesized and decorated with $CoFe_2O_4$ magnetic nanoparticles (NPs) via co-precipitation method. Systematic characterisation has been carried out to probe the structural and magnetic properties of the nanocomposite. The photocatalytic performance of the as-prepared $CoFe_2O_4$ decorated 3D TiO_2 nanocomposite was compared to that of commercial rutile-phase TiO_2 nanoparticles and pure 3D urchin-like TiO_2 microparticles. In order to evaluate its longevity in photocatalytic performance, the magnetically-assisted separation technique was employed to retrieve this nanocomposite, and a sequential recyclability test was conducted.

2. Experimental

2.1 Chemicals

All reagents used for this study were of analytical grade and used without further purification. The reagents used consist of titanium tetrachloride ($TiCl_4$, Merck Co.), tetrabutyl titanate (TBT, Sigma Aldrich), ethanol (95%, Merck) toluene (99.8%, Merck Millipore), ferric chloride and cobalt chloride (98% purity) and sodium hydroxide. Methylene blue (MB, molecular formula: $C_{37}H_{27}N_2Na_2O_9S_3$, R & M Chemicals, 1% aqueous solution) was chosen as a model of organic dye in this study for the evaluation of photocatalytic activity. Double distilled water was used for all dilution and sample preparations.

2.2 Synthesis of 3D urchin-like TiO_2

In a typical synthesis, there are two stages involved to synthesise pure 3D urchin-like TiO_2, as clearly illustrated in Figs. 1a and 1b.[18] Firstly, titanium tetrachloride ($TiCl_4$) was dissolved into distilled water in an icy bath under vigorous agitation to obtain a 50 wt% of $TiCl_4$ homogeneous aqueous solution. Separately, 4 mL of tetrabutyl titanate (TBT) was added into 30 mL of toluene in an icy bath at a separate reaction flask. Subsequently, 4 mL of $TiCl_4$ aqueous solution was added dropwise into the TBT/toluene solution under magnetic stirring. The mixture was continuously stirred for 1 hour. After 1 hour, a white precipitant was formed and was then transferred into a 50 mL cavity of stainless steel Teflon-lined autoclave (Fig. 1b). The temperature was held at 150 °C for 24 hours. After 24 hours, the product was collected and alternately washed with ethanol and distilled water to obtain the white precipitate (labelled as 3D TiO_2).

2.3 Decoration of $CoFe_2O_4$ nanoparticles onto 3D urchin-like TiO_2

Separately, 3D urchin-like TiO_2 was pre-synthesised, as mentioned in Section 2.2. The as-obtained 3D-TiO_2 was co-precipitated with Co^{2+} and Fe^{3+} crystalline salts in the presence of NaOH. By referring to Fig. 1c, about 0.2 g of 3D urchin-like TiO_2 was dissolved into a mixture of ethanol/DIW of 60 wt%. The titania suspension was magnetically stirred in a three-neck reactor under a nitrogen blanket for 30 minutes.

Subsequently, cobalt chloride and ferric chloride solution with a 1:2 molar ratio were prepared, and the respective solution was added simultaneously into the nitrogen flow titania suspension containing 3D urchin-like TiO_2. Under constant stirring for 1 hour, the temperature of the mixture was slowly adjusted to 80 °C. An alkaline NaOH solution was prepared with the proportion of molar ratio of 8 (with the reference of molar ratio of Co^{2+}:Fe^{3+} is 1:2). Carefully, the prepared NaOH solution was slowly added into the mixture and constantly stirred at 80 °C for 1 hour. The magnetic nanoparticles ($CoFe_2O_4$) were allowed to form in situ onto the surface of 3D urchin-like TiO_2 via a co-precipitation reaction. After the reaction, the magnetically decorated 3D urchin-like TiO_2 was washed and recovered alternatively using ethanol and DI water for several cycles. The $CoFe_2O_4$ nanoparticles decorated 3D TiO_2 structures were proposed.

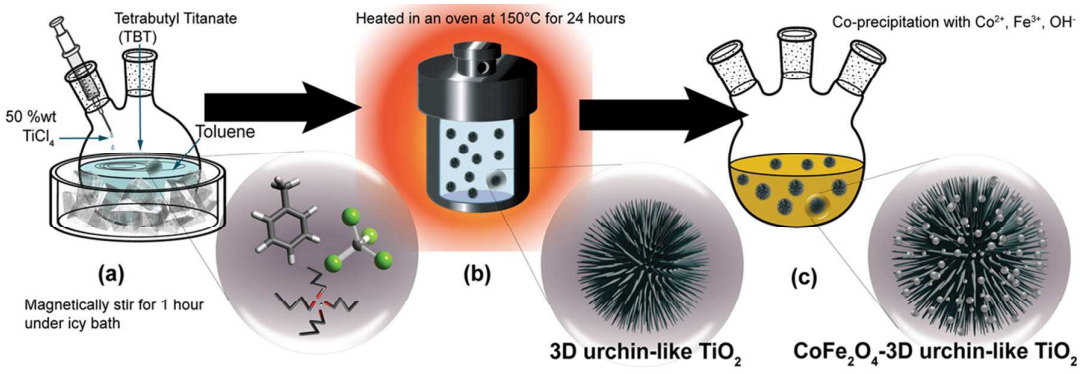

Fig. 1 Schematic diagram showing the preparation steps (a) the stabilisation procedure under icy bath with the addition of as-prepared titanium tetrachloride solution of 50 %wt, tetrabutyl titanate (TBT) and toluene serves as solvent. The mixture is magnetically stirred for 1 hour before transfer into Teflon-lined autoclave; (b) the mixture is poured into autoclave and heated in an oven at 150 °C for 24 hours to synthesis 3-dimensional urchin-like TiO_2; (c) preparation of $CoFe_2O_4$ nanoparticles decorated 3D urchin-like TiO_2 via co-precipitation of Co^{2+}, Fe^{3+} ions under alkaline condition (labelled as $CoFe_2O_4$-3D urchin-like TiO_2 nanocomposites)

2.4 Instrumental characterisations

The morphologies of the as-prepared nanomaterials were observed by using a high resolution transmission electron microscope (HRTEM, JEOL JEM-2100F) and ultra-high resolution field-emission scanning electron microscope (FESEM, Hitachi SU8000). In order to elucidate the crystal structure, the samples were characterised by the powder X-ray diffraction (XRD) patterns at a PANalytical EMPYREAN X-ray diffractometer (Cu K_a irradiation (40 kV/35 mA), in which the scanning rate of 1°/min in the 2θ range of 10–80° was employed. The adsorption isotherms of nitrogen were determined using an automatized micromeritics ASAP 2020. The BET surface area was obtained from these isotherms using the values of adsorption for P/P_0. The as-synthesised TiO_2 samples were further determined in terms of their crystalline composition by indexing with a standard powder diffraction pattern. Raman scattering was adopted to investigate the phases of the TiO_2 nanocrystals. The Raman spectra was obtained by using a Renishaw inVia Raman Microscope with the use of an objective lens of 50x (UV), and the laser source was selected at 532 nm under standard confocality. In this study, there are three parameters to be adjusted: exposure time, laser power and accumulation of scan in order to optimise the spectrum. For the magnetic properties measurements, a vibrating sample magnetometer (VSM LakeShore 7400) was employed to investigate the magnetisation curves. UV-visible absorption spectra of the samples were recorded on Perkin-Elmer Lambda 750 UV-VIS-NIR spectrophotometer. A photoluminescence study was carried out by using Renishaw inVia with the laser source selected at 325 nm to probe the optical transitions of the samples.

2.5 Photocatalytic activity tests

The photocatalytic activities of the as-prepared samples were evaluated by a designed photocatalytic reactor system, which is schematically shown in Fig. S1. The as-prepared photocatalysts were used to degrade aqueous solutions of MB, a commonly used model organic dye for evaluation of photocatalytic activities under UV-light irradiation. There are five sets of 8W ultraviolet Hg lamp (Sankyo Denki G8T5) with the maximum light intensity at 254 nm as the light source. A magnetic stirrer was used to control the agitation speed during the photocatalytic reaction. The samples (20 mg)

were each suspended in a test tube of 5 ml per volume of MB (initial concentration of 5 ppm) aqueous solution. Firstly, the suspensions were stirred for about 24 hours in the dark to achieve the adsorption-desorption equilibrium completely. This is to minimise the effect of the adsorption of the photocatalysts and self-decomposition of MB. Typically, there are five sets of photocatalytic experiments prepared in this study. Each sample was conducted by using 5.0 mL MB aqueous solution in a heavy-duty Schott soda-lime test-tube (GL-18) under constant UV irradiation. One test tube is reserved as a blank sample (uncatalyzed MB aqueous solution). Subsequently, the samples were irradiated by using a UV source at an irradiation distance of 5 cm, with the average intensity of UV irradiance measured to be 100 J/cm^2. The sample was irradiated continuously for 6 hours and the irradiation was repeated for different sets of samples. With sequential monitoring within an hour, the test tube sample was taken out from the radiation chamber and centrifuged at 4000 rpm for 45 min to sediment the photocatalyst. The supernatant of the sample was cautiously transferred into a quartz cuvette and was measured with a UV-visible spectrometer to monitor MB concentration by taking the maximum absorption at the wavelength of 665 nm, as this peak is assigned to be the dominant peak of MB. The procedures were repeated for $CoFe_2O_4$ nanoparticles decorated 3D urchin-like TiO_2 nanocomposites, commercial TiO_2 of rutile phase and $CoFe_2O_4$ nanoparticles, respectively.

3. Results and discussion

In the following section, the characterisations of the pure 3D urchin-like TiO_2 and $CoFe_2O_4$ decorated 3D urchin-like TiO_2 nanocomposites as well as their respective photocatalytic activity are discussed accordingly.

3.1 Morphology

3.1.1 3D urchin-like TiO_2

The formation of urchin-like TiO_2 stuctures can be envisaged by the following mechanistic explanation: Ti^{4+} precursor was dissolved in distilled water separately in icy conditions without the exposure to the ambient condition. The extreme cold condition is applied here for minimizing the overall reaction rate especially on the kinetic aspect to prevent overfast hydrolyzation. Additionally, a small amount of polar

water molecules that are immicible with the non-polar toluene are introduced into the mixture for better controlled of the process. With an elevation in temperature, water molecules will start to diffuse away from the high-energy water/toluene interface as a result in minimizing of the system energy, which ultimately promote water molecules to diffuse through the vicinity of Ti^{4+} ions and initialize the reaction. At this moment, Ti^{4+} precursors are undergoing hydrolyzation with water at the water/toluene interface, resulting in the formation of a crystal nucleus in the reactant solution.[23]

The morphology of the synthesized 3D- pure urchin-like TiO_2 was first examined by electron microscopy and the particle morphology is given in the Supporting information Fig. S2. Fig. S2a shows the TEM image of as-synthesized pure 3D TiO_2 microparticles, which are all well-separated without any aggregation. A higher magnification (x10k) image shown in Fig. S2b revealed that the particles appear to be highly hierarchical structured in the form of urchin-like microsphere. A zoom-in view of the TiO_2 microsphere can be seen in Fig. S2c, which showed that the individual well-faceted TiO_2 exhibits long, thin, and well-defined rod shape in structure that are extended out from the microsphere. The nanorods are found to possesses average length of 286.3 nm and an average width of 25.5 nm with a flat-terminated tip as observed in Fig. S2c. HR-TEM image (Fig. S2d) disclosed highly crystalline nature of the nanorods with a lattice fringes that comprises of 3.238 Å which is correspond-well with the {110} plane. The bulk crystallnitiy of the microsphere as revealed in the selected area electron diffraction (SAED) pattern are represented in Fig. S2e. The SAED pattern fits with rutile phase TiO_2 and it is further confirmed that the urchin-like TiO_2 particles are indeed pure rutile TiO_2. According to Hanaor and Sorrell (2011), this crystalline phase is attributed to the high temperature-induced phase changes when the TiO_2 growth regime was under hydrothermal treatment.[17] In order to further confirm that urchin-like TiO_2 exists in a 3D structure, FESEM imaging has been conducted. Fig. S1f with the magnification of x100k. This crossviewed image indicates that sample with individual nanorods are protruding outwards, where an unfilled interstices between each nanorods are clearly visible. In addition, the individual nanorods are self-assembled into a bunch-like structure with moderate compactibility. As compared to those of highly compact microspheres TiO_2 particles, such well-hierarchical nanostructure is believed to enhance the photocatalytic degradation activity of dye molecules due to abundance of surface area as well as the interstices that allows the

diffusion of the dye molecules to have direct contact with the nanorods and subsequently being adsorbed on its surface for subsequential photocatalytic reaction.

3.1.2 $CoFe_2O_4$ nanoparticles

A co-precipitation technique has been employed in synthesising $CoFe_2O_4$ nanoparticles for decoration on the 3D urchin-like TiO_2 microparticles. However, in order to understand the possible particle morphology of $CoFe_2O_4$, a controlled synthesis of $CoFe_2O_4$ nanoparticles had been carried out. Fig. S3a shows the low magnification TEM images of the $CoFe_2O_4$ nanoparticles that are spherical in shape and the size distribution is found to be fallen within the range from 1 nm to 11 nm. The polydispersity value of 38.20 % is calculated and represented in a histogram which is depicted in Fig. S3b. Fig. S3c shows the HRTEM image of a $CoFe_2O_4$ single particle that reveals the characteristic lattice fringes. The calculated d-spacing of 2.078 Å and 1.923 Å can be indexed to {400} planes and {331} planes, respectively. The SAED pattern and the corresponding intensity profile depicted in Fig. S3d indicate that the primary nanoparticles are well-fingerprinted with a pure $CoFe_2O_4$ phase.

3.1.3 $CoFe_2O_4$ decorated 3D urchin-like TiO_2

Fig. 2a shows the bright-field transmission electron microscopy image of $CoFe_2O_4$ nanoparticles decorated 3D urchin-like TiO_2 microsphere. In contrast to pure urchin-like microsphere that has sharp and soft tips along the edges of the nanorods (Fig. S2b), the $CoFe_2O_4$ nanoparticles decorated microsphere (Fig. 2b) have not much variation on the morphology except its tips appear to be blunt and rough due to the occupancy of the $CoFe_2O_4$ nanoparticles which are randomly distributed. Fig. 2c reveals the cross-viewed image of the selected part in Fig. 2a, which shows that the particles are randomly dispersed throughout the surface of TiO_2 microsphere. For the sake of better illustration on the uniformity in $CoFe_2O_4$ nanoparticles distribution as well as for the complementary to the bright field images in Fig 2a and Fig 2c, high-angle annular dark field (HAADF) TEM image has been collected to distinguish the existence of $CoFe_2O_4$ nanoparticles on the TiO_2 matrix. The dark-field image in Fig. 2b and 2d show a clear contrast between $CoFe_2O_4$ nanoparticles and microsphere, where there is a distinguishable contrast for both of the compounds due to differences

in the electron scattering ability as a result of variation in mean atomic number Z. HAADF-TEM image gives atomic number contrast information that can be correlated to the existence of $CoFe_2O_4$ nanoparticles on TiO_2 matrix. With respect to this, $CoFe_2O_4$ particle that possess higher Z value as compared to TiO_2 structure render the brighter domains while the darker domains appear to be TiO_2 matrix. Moreover, there is a bright yet partially resolve contour along the circumference of microspheres, which implies the agglomeration has took place among the $CoFe_2O_4$ nanoparticles due to the clustering effect and high surface energy of nanoparticles.[24,25] On top of this, the as-acquired SAED pattern that is shown in Fig. 2e is well-indexed by the characteristic d-spacing for both of the $CoFe_2O_4$ and TiO_2 rutile phases, which further suggests the existence of $CoFe_2O_4$ crystallites are uniformly distributed all over the TiO_2 rutile phase matrix. With respect to all of these structural analysis results, it is proved that current synthesis scheme is successfully in integrating $CoFe_2O_4$ nanoparticles onto the surface of urchin-like TiO_2 microspheres via co-precipitation process.

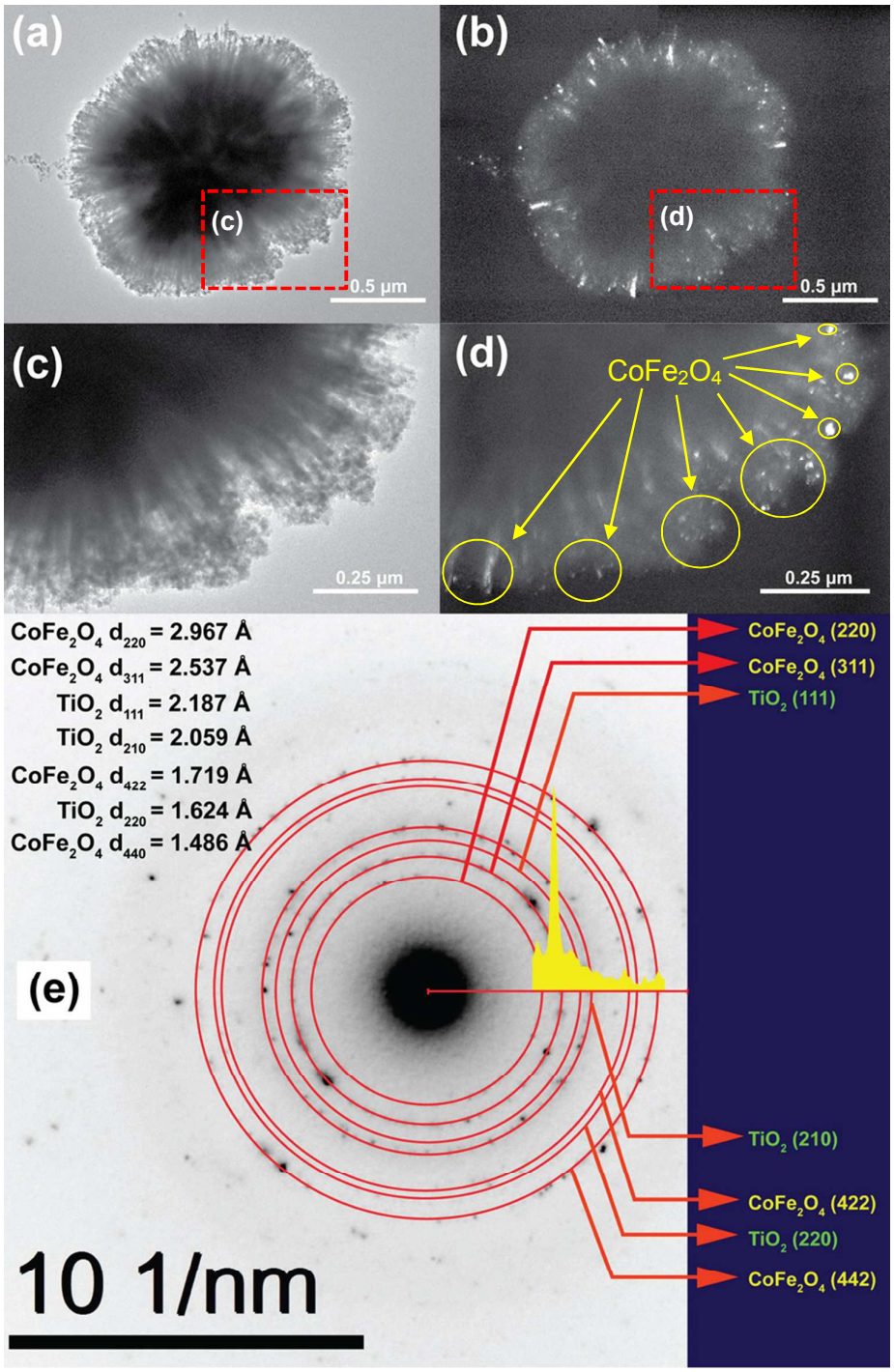

Fig. 2 Transmission electron microscopy (TEM) images of $CoFe_2O_4$ nanoparticles decorated 3D urchin-like TiO_2 photocatalyst of x10k magnification (a) bright field, (b) dark field. (c) and (d), respectively shows the closer view of the selection region in (a) and (b). (e) SAED pattern and intensity profile of the selected micrograph region in (a).

For a better comprehension of the interfacial bonding between $CoFe_2O_4$ nanoparticles with the rutile phase nanorods, high resolution HR-TEM images have been provided in Fig. 3a-3d. A selected region of Fig. 3a (upper right) illustrated the spot where $CoFe_2O_4$ nanoparticles and TiO_2 nanorods are attached together. Three distinctive regions (region 1-3) have been selected to view the lattice fringes of the structure and the possible changes occurred in the atomic level after the integration of $CoFe_2O_4$ nanoparticles. As noted in Fig. 3b (region 1), the intensity profile observed for the line drawn in Fig. 3b, which traces the atomic layers a the crystalline rod shows clear and continuous lattice fringes with an interplanar spacing of about 0.328 nm which corresponds to the (110) lattice spacing of rutile structure of titania. The fast Fourier transform (FFT) pattern (inset of Fig. 3b) is of rutile phase of TiO_2 with the zone axis diffraction of $[1\bar{1}0]$. Beyond this region, it can be seen that in Fig. 3c (region 2) the TiO_2-$CoFe_2O_4$ interface displays two sets of lattice fringes evidenced to be d_{110} = 0.322 nm of rutile phase titania and d_{331}= 0.193 nm of $CoFe_2O_4$. At the TiO_2/$CoFe_2O_4$ interface, atomic arrangement is disoriented and this could be of the lattice mismatch as a result of introduction of new chemical compound such as $CoFe_2O_4$ into the TiO_2 during the stage of co-precipitation. Studies have shown that this always happens for the hetero-junction interfacial materials that made of two different compounds.[26,27] The lattice mismatching and disorientation happen that could be ascribed to the defect found in the atomic levels. This defect often is associated with the different chemical potential of the secondary compound that resulting the lattice re-arrangement by adjusting its lattice spacing in a newly ordered crystalline structure. Moreover, the corresponding FFT pattern of the interface (inset Fig. 3c) displays a unique in-between diffraction pattern of $CoFe_2O_4$ and TiO_2 phases. Conclusive evidence can be drawn by referring to the indexed diffraction spots which indicating white arrows represent the diffraction spots of TiO_2 rutile phase at $(\bar{1}\bar{1}\bar{1})$ and (110), while the yellow arrows ascribed to the $CoFe_2O_4$ diffraction spots at (200) and $(\bar{1}11)$. Further observation at region 3 (Fig. 3d), however, distinctly revealed the structure of $CoFe_2O_4$ with interplanar spacing of 0.484 nm that corresponds to (111) plane of lattice orientation. The FFT analysis over the $CoFe_2O_4$ region shows a typical diffraction pattern which can be indexed to be (400), $(\bar{1}11)$, $(\bar{1}\bar{1}\bar{1})$, $(\bar{2}00)$ and (022) crystal planes viewed along the $[01\bar{1}]$ zone axis of $CoFe_2O_4$. The diversification in the

FFT patterns of these three regions indicates that the magnetic $CoFe_2O_4$ nanoparticles have been successfully decorated on the urchin-like structure of TiO_2.

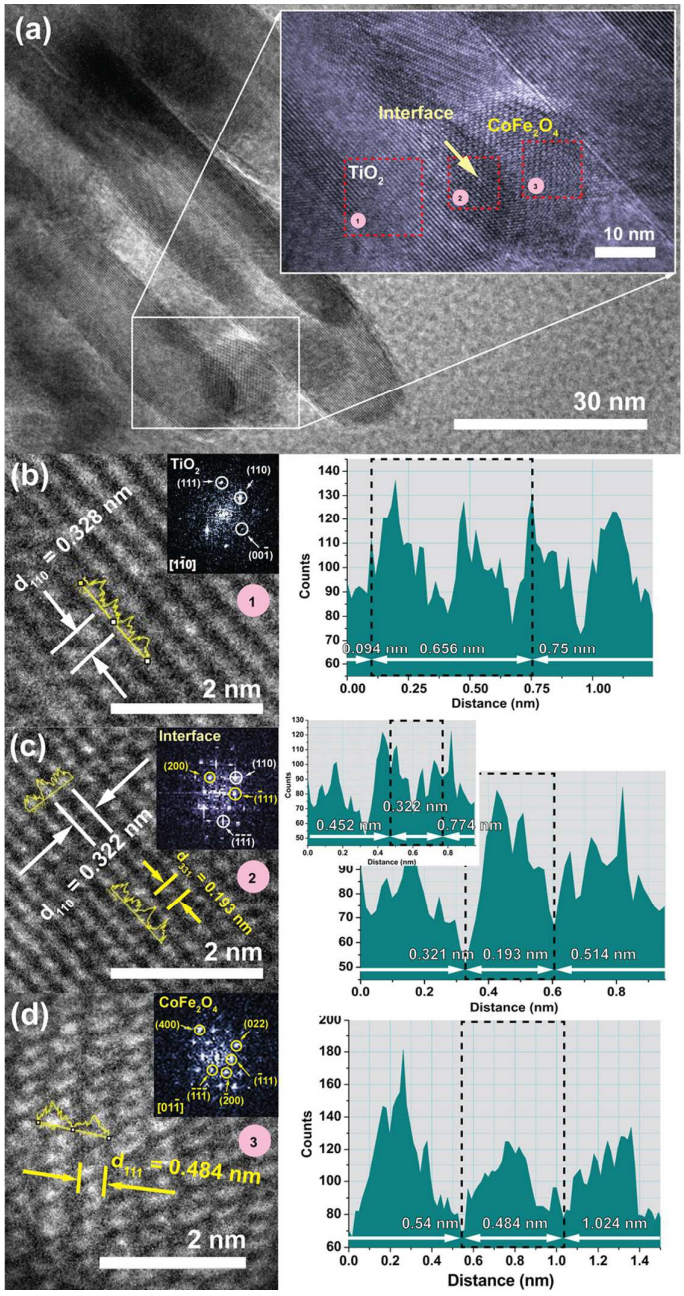

Fig. 3 (a) High resolution TEM images of $CoFe_2O_4$ nanoparticles decorated 3D urchin-like TiO_2 structure. The magnified region showing the interface of a typical nanorod of urchin-like TiO_2 and a seeding $CoFe_2O_4$ nanoparticles on the surface of TiO_2 nanorods. (b)-(d) represent the high magnification of HR-TEM images (x800k) and the line intensity profiles across the TiO_2-$CoFe_2O_4$ interface (from region 1-3), corresponding to the line drawn in (b), (c) and (d), respectively. Insets: the correspondent fast Fourier transform (FFT) patterns in (b), (c) and (d).

In addition to HRTEM imaging, the scanning transmission electron microscopy (STEM) elemental mapping has been conducted and the resulting elemental maps are depicted in Fig. 4. The different elemental distribution, which consists of Ti, O, Co and Fe (Figs. 4a – 4f) clearly shows that the $CoFe_2O_4$ nanoparticles are present on the 3D urchin-like TiO_2 structure. It is noteworthy that the distribution of each element was uniform throughout the surface of the TiO_2 microsphere. These results indicate that $CoFe_2O_4$ nanoparticles have been successfully decorated on the 3D urchin-like TiO_2 via the co-precipitation method. With the $CoFe_2O_4$ nanoparticles decorated hierarchical 3D urchin-like TiO_2, it is suggested that the magnetic properties that are owned by $CoFe_2O_4$ nanoparticles could be harnessed to enable the magnetically retractable feature to take place upon photocatalytic reaction. Under the identical preparation method of 3D urchin-like structure of TiO_2 microsphere, the 3D TiO_2 particle produced has wide particle size distribution (see Supporting Information S4). We declare that the particle size is ranging from less than 100 nm to more 1 μm. In addition, in-situ co-precipitation of $CoFe_2O_4$ nanoparticles is carried out with the use of as-prepared 3D urchin-like TiO_2 microspheres and there is a probability that the 3D urchin like TIO_2 microspheres could be in different size range being imaged during the TEM- elemental mapping characterization (Fig. 4).

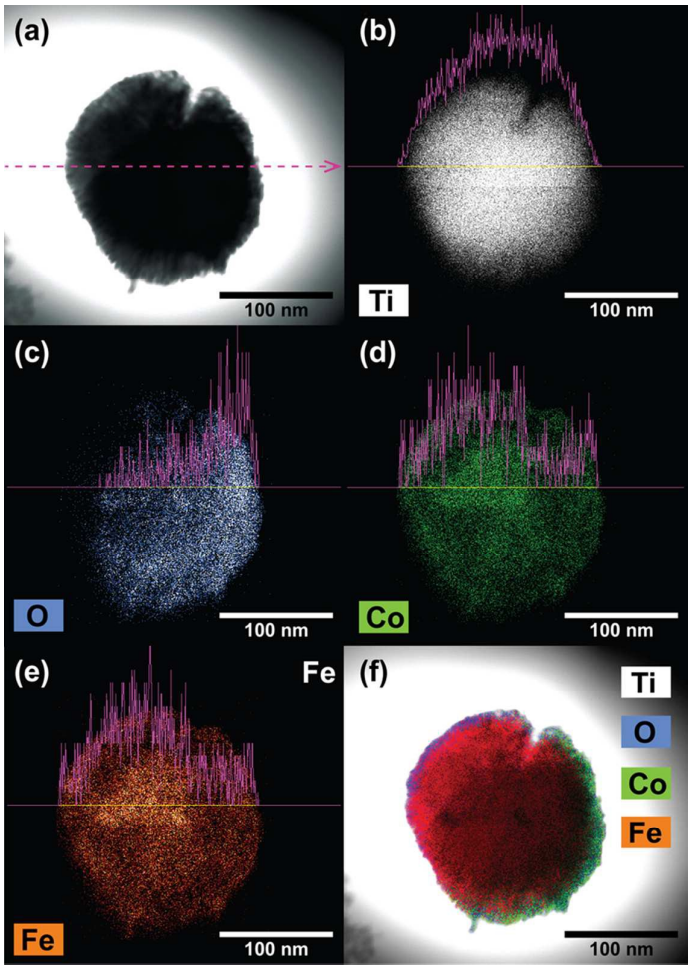

Fig. 4 $CoFe_2O_4$ decorated 3D urchin-like TiO_2 (a) electron image with elemental line scan overlaid onto the TEM image of (b) Ti map, (c) O map, (d) Co map, (e) Fe map and (f) combination Ti + O + Co + Fe maps for the ROI.

3.2 Phase structures

Fig. 5 shows the XRD pattern for the constituents and the $CoFe_2O_4$-3D TiO_2 nanocomposites. All of the peaks are in good agreement with the standard spectrum (JCPDS no.: 21-1276 for rutile-phase TiO_2 and 22-1086 for $CoFe_2O_4$). It can be seen that from Fig. 5a–5c, XRD patterns exhibit strong diffraction peaks at 27.53°, 36.22°, 41.38°, 54.44° and 64.18°, indicating the hydrothermally prepared 3D urchin-like TiO_2 particles are in the rutile phase. Noticeably, there are compound peaks present especially at 2θ = 35.54°, 43.17°, and 57.36°, which could be indexed to be (311), (400) and (422) Miller indices of $CoFe_2O_4$. Additionally, humps appeared that could be clearly distinguished from the spectrum of Fig. 5c (3D urchin-like TiO_2), especially at

2θ = 18.44°, 46.65° and 74.23°. The broadening of the peaks was mainly attributed to the nanosized $CoFe_2O_4$ present in the sample, which is in agreement with TEM and HRTEM results depicted in Fig. 2 and Fig. 3.[28] These results conclude that the nanocomposite is composed of $CoFe_2O_4$ and TiO_2 with rutile phase that has been successfully prepared. Visible evidence presented in the insets respectively prove that the as-prepared white powder of pure 3D urchin-like TiO_2 was indeed successfully integrated with $CoFe_2O_4$ nanoparticles to produce the magnetic photocatalyst nanocomposites, represented by the greyish colour powder.

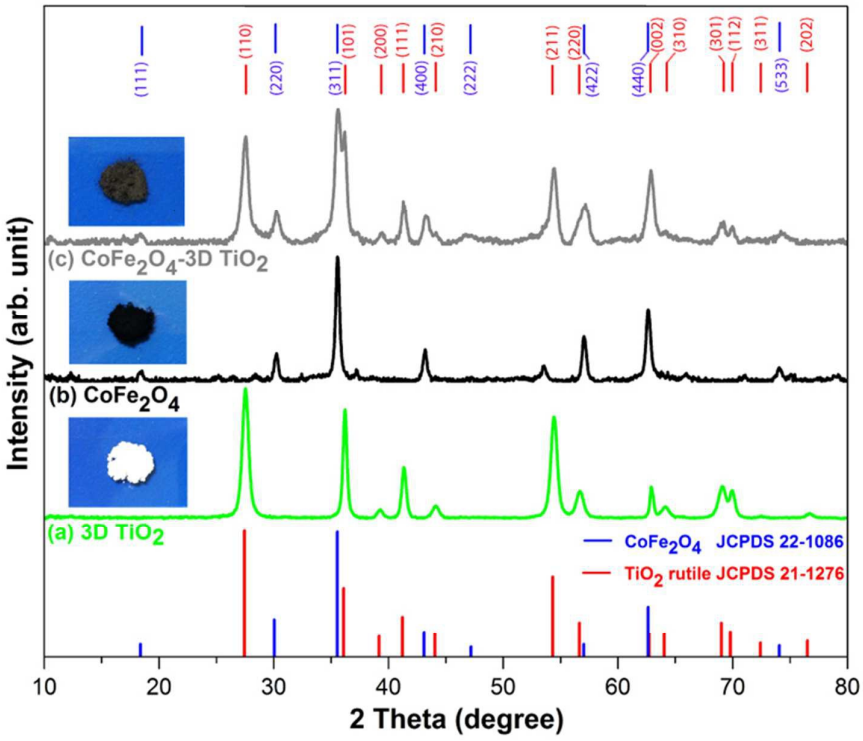

Fig. 5 X-ray diffraction (XRD) patterns of (a) 3D urchin-like TiO_2, (b) $CoFe_2O_4$ nanoparticles, and (c) $CoFe_2O_4$ decorated 3D urchin-like TiO_2

3.3 Raman results

Raman measurement was performed to probe the internal structure of the TiO_2 photocatalyst prior and after the decoration of $CoFe_2O_4$ nanoparticles. In the measurement, all the measurement conditions such as laser power (50 %), acquisition time and signal accumulation were kept the same to ensure the comparison of the

spectra can be done. Fig. 6a demonstrated the presence of rutile phase for pure 3D urchin-like TiO_2. The bands located at 456 and 622 cm^{-1} can be seen in Fig. 6a, exhibiting the two-phonon scattering with E_g and A_{1g} modes of rutile structure.[29-32] Investigations show that the peak at 456 cm^{-1} could be due to the degeneration of E_g peak as a result of symmetric bending of O-Ti-O in {001} plane of opposite movement of O atoms across O-Ti-O bonds.[33] On the other hand, the peak appearing at 622 cm^{-1} (A_{1g}) that could be explained by the symmetric stretching of O-Ti-O bond in {110} plane. The broad Raman peak at around 248 cm^{-1} could be ascribed to the second order scattering or disorder effects upon the interaction of laser with the TiO_2 microspheres.[34-35] These results implies that the as-synthesised pure 3D urchin-like TiO_2 indeed consists of a rutile crystal structure. Meanwhile, the Raman spectrum of $CoFe_2O_4$ is represented in Fig. 6b. After careful analysis, it would be possible to observe Raman bands at 183, 318, 475, 574, 629 and 692 cm^{-1}. It should be noted that the Raman vibrational modes below 600 cm^{-1} are ascribed to the vibrations of oxygen within the octahedral site, while 600 cm^{-1} can be assigned to vibrations within tetrahedral sites.[36] A relatively weak shoulder peak near 183 cm^{-1} which is attributed to the T_{1g} mode is related to the translational motion of the whole tetrahedron in $CoFe_2O_4$ sub-lattice. The most intense peak at 318 cm^{-1} is due to symmetric bending of Fe-(Co)-O bonds that is assigned to be E_g mode. Two more peaks appear at 475 and 574 cm^{-1} which are of $T_{1g}(2)$ and $T_{1g}(1)$, respectively that can be the asymmetric stretching of Fe-(Co)-O bonds in the octahedral site mode.[37] Raman bands at 629 and 692 cm^{-1} are of $A_{1g}(2)$ and $A_{1g}(1)$, respectively is due to the symmetric vibrations of the metal in the tetrahedral site of $CoFe_2O_4$.[38] Many salient peaks emerge in the sample of $CoFe_2O_4$ integrated TiO_2 nanocomposites (Fig. 6c), prominently at 311, 442, 573, 621, 691 cm^{-1}. Interestingly, upon the integration of 3D TiO_2 matrix with $CoFe_2O_4$, the intensity of the peak at ~182 cm^{-1} appears to be lowered. Such appearance is deduced to be the introduction of $CoFe_2O_4$ on the TiO_2 surface that causes lattice mismatch due to the existence of two different compounds of the $CoFe_2O_4$-TiO_2 interface. Taking into consideration of irradiation of the whole crystal structure at this interfacial region, the Raman vibrational modes might be different and this might hinder the appearance of the peak. Moreover, the manifestation of both peaks at 442 and 621 cm^{-1} could be ascribed to the lattice strain or lattice defects mainly due to the presence of $CoFe_2O_4$ nanoparticles, which profoundly contribute in Raman shifting. The peaks at around 475 and 629 cm^{-1} which belong to $CoFe_2O_4$ bands in Fig. 6c are hardly seen due and

suppressed by dominant peaks of 442 and 621 cm^{-1} that belongs to TiO_2. Furthermore, the black appearance of $CoFe_2O_4$ that render relatively weak peak intensity also contribute to this phenomenon.

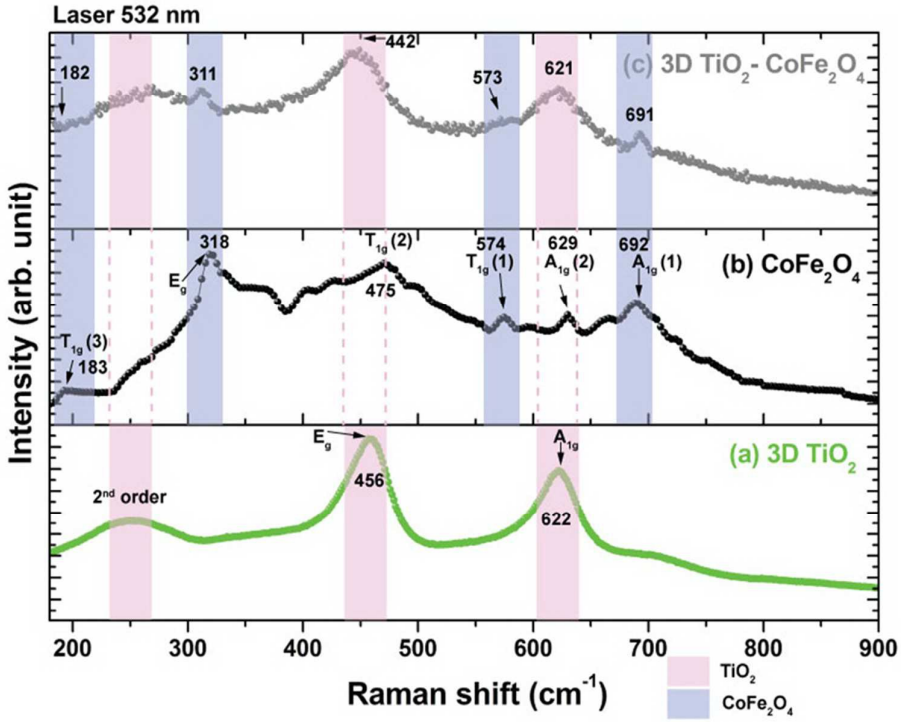

Fig. 6 Raman spectra of (a) 3D urchin-like TiO_2, (b) $CoFe_2O_4$ nanoparticles (c) $CoFe_2O_4$ decorated 3D urchin-like TiO_2 nanocomposites.

3.4 Magnetic properties

Further elucidation on the room temperature magnetic hysteresis loops of $CoFe_2O_4$ and $CoFe_2O_4/TiO_2$ nanocomposite is presented in Fig. 7. The values of coercive force (G) and saturation magnetisation (Ms) of the $CoFe_2O_4$ nanoparticles are 311.98 G and 0.795 emu/g, respectively. On the other hand, the coercivity and saturation magnetisation of the nanocomposite were measured to be 408.62 G and 0.211 emu/g, respectively. The lower saturation magnetisation in the nanocomposite could be attributed to the presence of diamagnetic TiO_2 in the sample that contributes to the overall mass fraction.[39] It is worth pointing out that the presence of magnetic nanoparticles in TiO_2 photocatalysts was crucial in this study as it enables the facile separation of the as-synthesised nanocomposite under the presence of an applied

magnetic field (inset Fig. 7). This is important because the magnetically active nanocomposite can be recycled and reused for sequential usage in wastewater treatment.

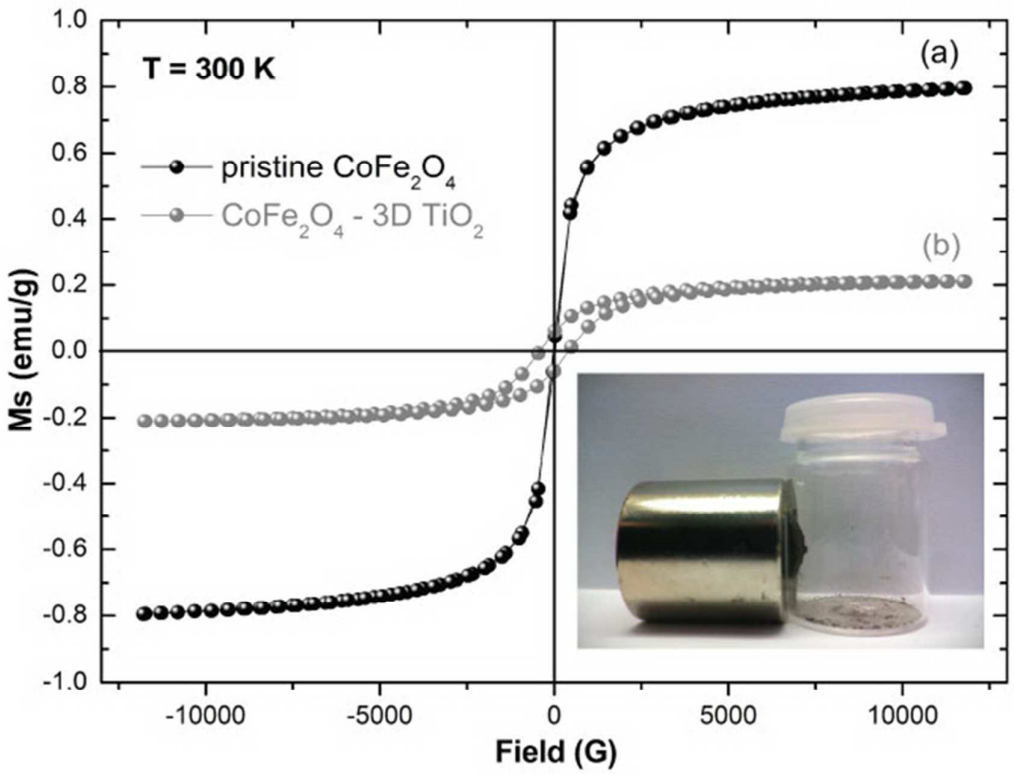

Fig. 7 Magnetic properties of (a) $CoFe_2O_4$ nanoparticles and (b) $CoFe_2O_4$ decorated 3D urchin-like TiO_2 nanocomposites. Inset shows the magnetic responsiveness of $CoFe_2O_4$-3D urchin-like TiO_2 with external magnetic field measured at room temperature 300K.

3.5 Optical properties

The optical absorption of pure 3D urchin-like TiO_2, $CoFe_2O_4$ and $CoFe_2O_4$ decorated 3D urchin-like TiO_2, are shown in Fig. 8a–8c, respectively. Fig. 8a shows that the as-synthesised 3D hierarchical urchin-like TiO_2 exhibits high absorption in the UV region, and the absorption edge of 3D TiO_2 was at about 378 nm. For $CoFe_2O_4$ nanoparticles (Fig. 8b), there is a broad and obvious absorption that can be seen ranging from UV up to the visible region. For $CoFe_2O_4$ decorated 3D urchin-like TiO_2 nanocomposites (Fig. 8c), there is a strong, yet prominent absorption at a cut-off wavelength of 443.75 nm and the intensity of absorbance increases remarkably in the range of 300-600 nm

as compared to that of pure 3D urchin-like TiO_2, which indicates that the band edge absorption has been extended to visible light region after the introduction of $CoFe_2O_4$ nanoparticles. This is ascribed to the incorporation of Fe^{3+} ion (0.64 Å) and Co^{2+} ion (0.65 Å) into the oxide of Ti^{4+} ion (0.68 Å) has been occurred.[40,41] With the subsitutition for Ti^{4+} by Fe^{3+} or/and Co^{2+} ions into the lattice structure of TiO_2, there is a tendency where a new impurity level lower than the original conduction band of rutile titania is formed. Hence, the electronic transition from the valence band of TiO_2 towards this intermediate band with that are lower than original conduction band can take place. In addition to this, it is reported that the p-orbital of these foreign ions overlapped with the valence band O 2p-orbitals also up-shift the valence band which finally narrowing the gap with respect to the conduction band.[42] Hence, the electronic transitions between the impurity level and the valence or conduction band will thus red shifted and finally render the smaller optical bandgap and upshifting the absorption cut-off to longer wavelength.[43] Such enhancement in overall absorption is vital in further improving the photocatalytic performance, which is depicted afterwards.

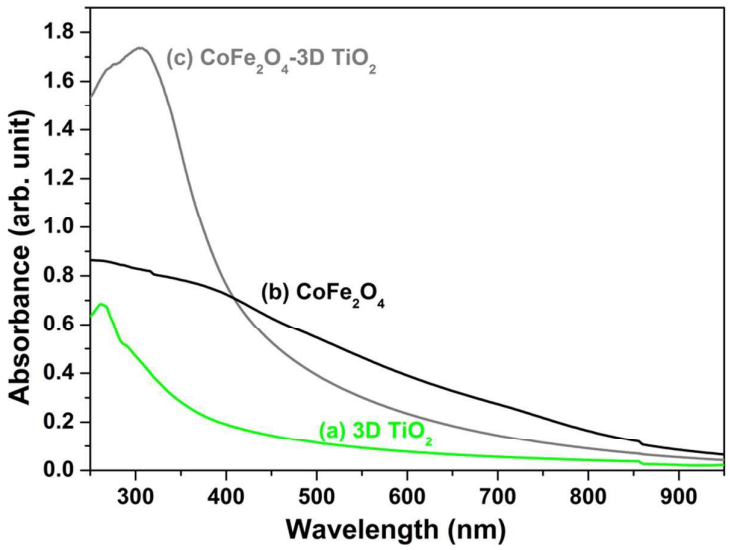

Fig. 8 UV-vis absorbance spectra (a) 3D urchin-like TiO_2, (b) $CoFe_2O_4$ nanoparticles, and (c) $CoFe_2O_4$ decorated 3D urchin-like TiO_2 nanocomposites

In addition to UV absorbance results, a photoluminescence (PL) study has been carried out to probe the tendency of electron-hole recombination rate for all the samples as shown in Fig. 9. When there is an adequate incoming photon energy is

absorbed by the electrons on valence band (VB), they can further be excited to a higher level in conduction band (CB). This process proceeds to recombination, where the electrons and holes are recombined and causes the emission of light. The intensity of emitted light is directly correlated with the recombination rate of electron and holes and thus can shed light on the lifetime span of the charge-carriers. Fig. 9a has the highest intensity among the three samples. This is followed by Fig. 9b (3D urchin-like TiO_2) and Fig. 9c. The lowest photoemission intensity of $CoFe_2O_4$-TiO_2 nanocomposites is ascribed to the least probability of electron and hole to recombine and emitting light. Possible lower recombination rate of electron-hole in the nanocomposite is of the non-radiative type (Shockley-Read-Hall) of recombination as a result of impurities level found in the nanocomposite structure. The Fe^{3+} and Co^{2+} exist in the TiO_2 lattice structure create the defect levels in the forbidden gap of TiO_2 causes the photoinduced electron in CB will move to these extra levels before returning to the VB followed by the emission of photons.[44] Hence, it could be deduced that magnetic nanocomposites have the lowest electron-hole recombination efficiency, which ultimately contribute to the enhancement of overall photocatalytic performance if compared to the pure 3D urchin-like TiO_2.

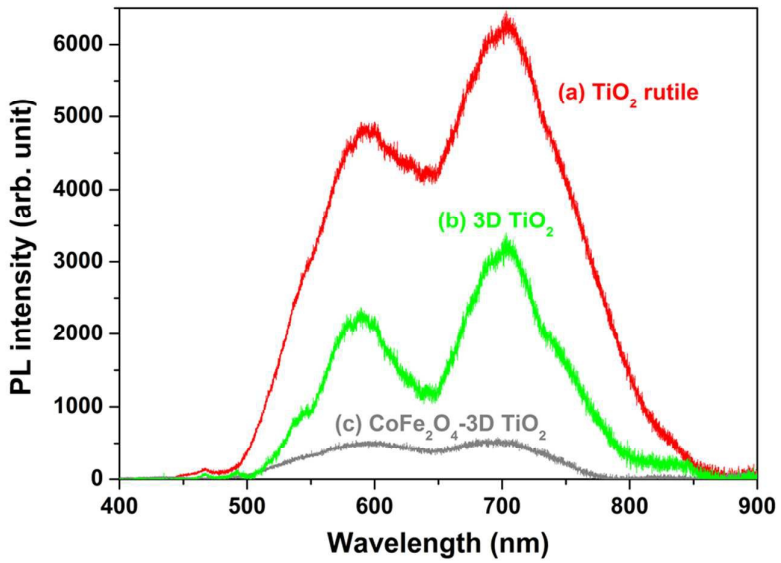

Fig. 9 Photoluminescence spectra of (a) commercial TiO_2 rutile, (b) 3D urchin-like TiO_2, and (c) $CoFe_2O_4$ decorated 3D TiO_2 nanocomposites.

3.6 Photocatalytic performance of methylene blue (MB)

Fig. 10 shows the absorbance of the MB solution under UV light for different time intervals, where the changes of the MB maximal absorbance at wavelength (λ = 665 nm) with and without the addition of photocatalyst were studied. The concentration of MB suspensions for each sample was monitored every hour by examining the maximal absorbance of MB with a UV-visible spectrophotometer. For the blank sample, there is only a slight decrease in the absorbance peak observed at 665 nm, even though after 6 hours of irradiation and the maximal absorbance at the sixth hour still remains as high as ~95% of the original MB (Fig. 10a). In this process, the photodegradation activity of the uncatalyzed MB solution was only triggered by UV light. It was quantitatively evidenced that the percentage of MB being removed is increased with respect to irradiation time. As a comparison, an evaluation of photocatalytic performance of commercial rutile phase TiO_2 was also conducted (Fig. 10b). It was observed that the maximal absorption peak at 665 nm was reduced for these samples. According to the result, the MB that underwent photodegradation increased to 46.71 % after 6 hours of irradiation, which is two times higher than that of the uncatalyzed sample (Fig. 10a).

On the other hand, the photocatalytic degradations of MB over different time intervals by using the as-synthesised 3D urchin-like TiO_2 are shown in Fig. 10c. Upon the UV irradiation up to 6 hours, the percentage of MB removed under the presence of pure 3D urchin-like TiO_2 is greatly reduced up to 79.91%, which is almost two times higher as compared to that of commercial rutile TiO_2 (45.54 % left of MB) in Fig. 10b. Such enhancement could be due to the high surface area to volume ratio endowed by the hierarchical structure of urchin-like TiO_2, which provides excellent accessibility for the water molecules to diffuse into the space between the nanorods of the urchin-like structure. As a consequence, a large number of hydroxyl radicals are produced and this has greatly assisted in triggering the degradation process.[45-48] For this batch of samples, the maximal absorption of MB at 665 nm at the 6^{th} hour is only 20.78% of the initial MB concentration.

For $CoFe_2O_4$-3D urchin-like TiO_2 nanocomposite, it is observed that 98.89% of MB successfully underwent photodegradation upon the 6^{th} hour of irradiation (Fig.

10d). It is hypothesised that the integration of $CoFe_2O_4$ nanoparticles onto the surfaces of urchin-like TiO_2 could synergise the photocatalytic activity in degrading the MB. Although the surface area of the nanocomposite was measured to be 42.38 m^2/g as compared to that of pure urchin-like TiO_2 (68.52 m^2/g), the nanocomposite still exhibits better photodegradation rate, which is more prevalent than pure urchin-like TiO_2. Such an enhancement can be ascribed the enhancement in charge separation efficiency for the nanocomposite, as evidenced by the photoluminescence measurement, which has been discussed in the previous section. Despite the BET value for the $CoFe_2O_4$-TiO_2 nanocomposites is lower than that of pure urchin-like TiO_2 particles, based on the photodegradation experiment of MB under the presence of the nanocomposite, there is an obvious enhancement of the photodegradation rate. This observation can be attributed to the integration of urchin-like TiO_2 with $CoFe_2O_4$ nanoparticles that contribute a synergistic effect in term of prolong life span of electron-hole separation, which will be discussed in detailed afterwards. On top of that, in order to evaluate the role of $CoFe_2O_4$ nanoparticles in the photodegradation process, the performance of pure $CoFe_2O_4$ nanoparticles was also examined. According to the result (Fig. 10e), it is observed that the absorption maxima for this sample attains 20.77% of initial MB concentration, where the overall performance still lags behind those of commercialised rutile TiO_2 and pure urchin-like TiO_2. Nevertheless, the feasibility of $CoFe_2O_4$ nanoparticles in partially photodegrading the MB in current study still needs further investigation. Fig. 10f illustrates the photodegradation rate for all the samples as a function of irradiation time. It was found that $CoFe_2O_4$-3D urchin-like TiO_2 nanocomposites exhibit the greatest photodegradation rate, with the graph obeying a hyperbolic growth pattern. The photodegradation rate for this sample is 1.2 fold than that pure 3D urchin-like TiO_2, whereas it is almost two times higher than that of commercial rutile TiO_2. On the other hand, the photodegradation performance for this sample is twenty times higher than uncatalyzed MB.

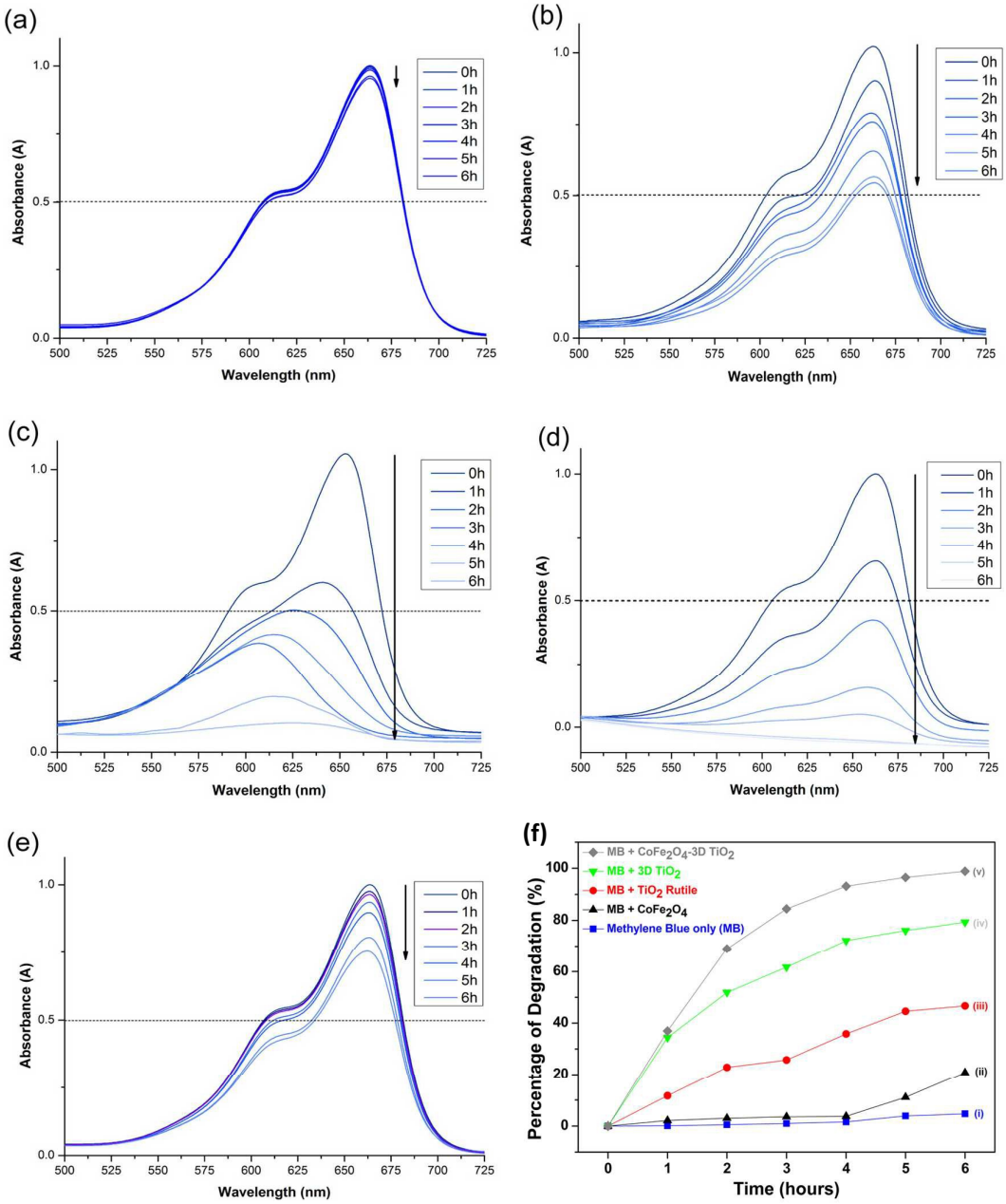

Fig. 10 Normalised time-dependent UV-vis optical absorbance spectra at maximal absorptions of wavelength (λ = 665 nm) for (a) uncatalyzed MB, (b) commercial rutile TiO_2, (c) 3D urchin-like TiO_2 photocatalyst added MB suspension, (d) $CoFe_2O_4$ decorated 3D urchin-like TiO_2 nanocomposites added MB suspension, (e) $CoFe_2O_4$ added MB suspension, and (f) degradation curves of different samples showing the efficiency of photocatalytic degradation of MB under constant UV irradiation.

In terms of a kinetic study (Fig. 11), the photocatalytic decomposition of MB by nanocomposite follows a pseudo-first kinetic law that can be expressed as

$$-\ln\left(\frac{C}{C_0}\right) = kt \quad (1)$$

where C is the reactant concentration at time t = t, C_0 is the reactant concentration at t = 0, k is the pseudo-first order rate constant and t is the time measured, respectively.[49] The relationship between ln (C_0/C) and irradiation time (t) for various samples are shown in Fig. 11. It is observed that all the graphs exhibit linear relationship between ln (C_0/C) and irradiation time. The pseudo-first-order rate constant, k are determined by calculating the gradient of the graph together with the corresponding linear regression coefficients (*R*) for different samples as depicted in Fig. 11. For the MB solution without any photocatalyst, the rate constant gave the k value of 0.00827 h^{-1} (Fig. 11a), and this value increased to 0.0321 h^{-1} for the sample with the addition of pure $CoFe_2O_4$ nanoparticles (Fig. 11b). Meanwhile, with the addition of commercialised TiO_2 of rutile phase, the k value ascends to 0.1073 h^{-1} (Fig. 11c) and the value further increased to 0.2605 h^{-1} for the pure 3D urchin-like TiO_2 (Fig. 11d). Finally, the photocatalytic degradation rate manifested by $CoFe_2O_4$ decorated 3D urchin-like TiO_2 nanocomposites attains the highest among all, with the *k* value of 0.7432 h^{-1}.

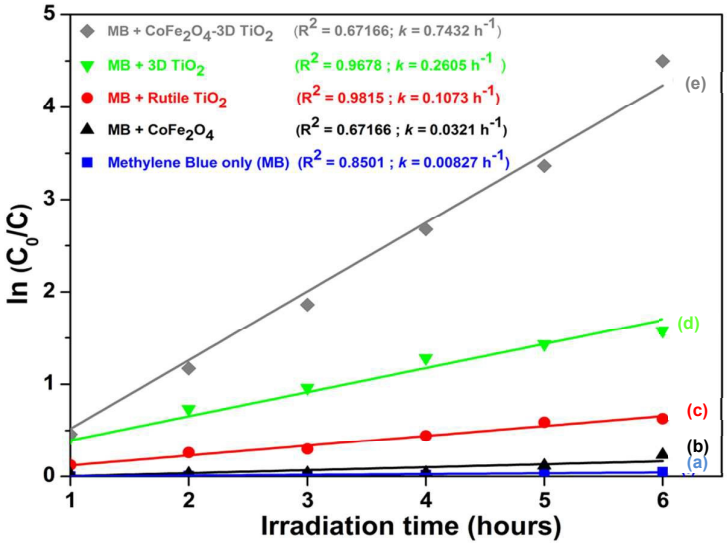

Fig. 11 Kinetics study of MB degradation (a) MB only, (b) $CoFe_2O_4$ added, (c) commercial TiO_2 of rutile phase, (d) 3D urchin-like TiO_2, and (e) $CoFe_2O_4$ decorated 3D urchin-like TiO_2 nanocomposite.

The underlying mechanism of the photodegradation process is represented in Fig. 12. Upon sufficient absorption of UV light, photo-excited electrons are created in rutile TiO_2 and transfer to its CB, leaving the holes in the VB, where both of these charge carriers are exist in the state of temporary entity of e^-/h^+ pairs (eqn (2)) that are bounded by column force. The strong interfacial connection between $CoFe_2O_4$ nanoparticles throughout the TiO_2 surfaces can extract the excited electrons in the CB of TiO_2 to transfer to that of $CoFe_2O_4$ and this promote the efficient charge separation at interfaces of the $CoFe_2O_4$-3D TiO_2, which in turn hinder their recombination (eqn (3)). According to Sathishkumar et al. (2013) and Xiong (2013), $CoFe_2O_4$ has a band gap of c.a. 1.1 eV, which is a visible active material.[50,51] The photoinduced electrons and holes are separated at the interface of the $CoFe_2O_4$-3D TiO_2 nanocomposites due to the decreased of the potential energy of $CoFe_2O_4$. Therefore, the photoinduced electrons are preferably injected from CB of rutile 3D TiO_2 to that of CB of $CoFe_2O_4$. This coupling structure can effectively reduce the electron-hole recombination probability and therefore increases the electron mobility, which enable the charge carriers to be transferred to the surface of the $CoFe_2O_4$. As the irradiation time is prolonged, the dissolved O_2 molecules will capture the electron on the $CoFe_2O_4$ surface to generate reactive superoxide radical anions ($O_2^{\bullet -}$) (eqn (4)). These radicals will subsequently contribute towards the photocatalytic degradation by converting the

methylene blue molecules to the by products such as CO_2 and H_2O (eqn (5)).[52] On the other hand, the photoinduced holes (h^+) are responsible for the oxidation reaction and the adsorbents (H_2O/OH^-) are effectively being oxidized by removing the electrons to form hydroxyl radicals (•OH) (eqn (6) and eqn (7)). Finally, these •OH radicals oxidize the MB dye molecules adsorbed to the degraded products (eqn (8)).[53] A plausible mechanistic scheme of the creation of the e^-/h^+ pair and the photocatalytic activity for the magnetic nanocomposite photocatalyst is shown below, and the illustration can be seen in Fig. 12.

TiO_2 (rutile) + $h\nu \rightarrow h^+ + e^-$ (2)

$CoFe_2O_4$-$TiO_2 \rightarrow CoFe_2O_4$-$TiO_2$ (e^-) (3)

$e^- + O_{2\ absorbed} \rightarrow \bullet O_2^-$ (4)

$\bullet O_2^- +$ MB dye $\rightarrow$ degraded products (5)

$h^+ + H_2O_{absorbed} \rightarrow H^+ +$ •OH (6)

$h^+ + OH^-_{absorbed} \rightarrow$ •OH (7)

•OH + MB dye $\rightarrow$ degraded products (8)

where an unpaired electron (radical) is represented by a point, a valence band electron hole is represented by h^+, and a conducting band electron is denoted by e^-.

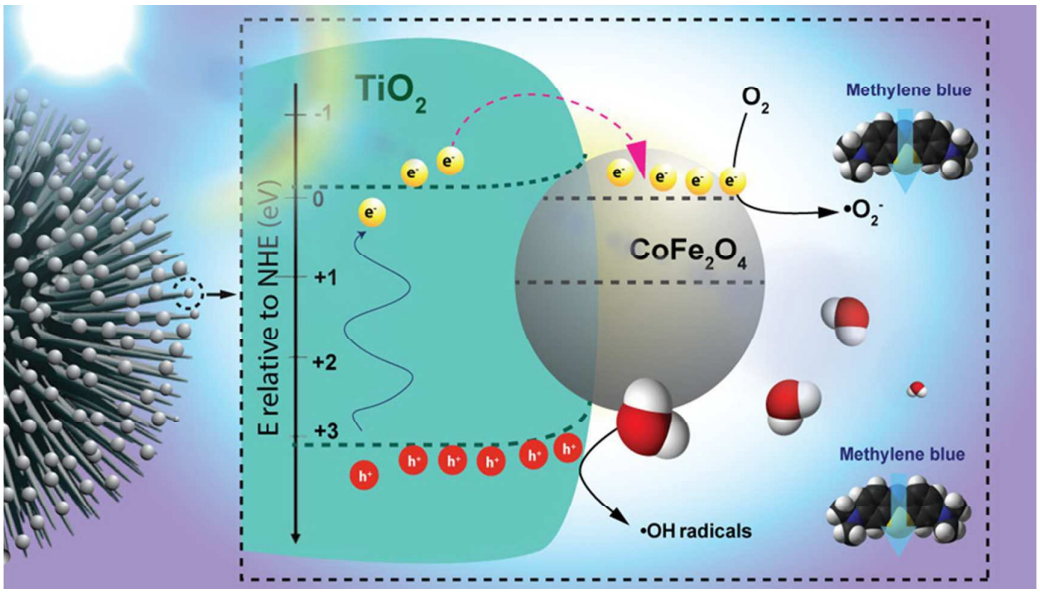

Fig. 12 Illustration of photocatalysis by $CoFe_2O_4$-3D urchin like TiO_2 nanocomposites.

3.7 Recyclability test

Recyclability of photocatalysts is one of the prerequisites to verify the practicality of a direct application of photocatalysts and to develop heterogeneous photocatalysis technology for wastewater treatment. The samples were subjected to photodegradation and retrieved back by applying 0.6 Tesla magnetic field up to five cycles (Fig. 13a). The photocatalytic degradation efficiency was 98.0% and 97.6% during the first and second cycles, respectively. The catalyst activity slightly dropped in the third cycle and fourth cycle, giving the efficiency of 95.0% and 94.5%. During the fifth cycle, a degradation efficiency of 93.8% was obtained. A better visualisation of temporal changes in MB concentration with the addition of magnetic photocatalyst is represented in Fig. 13b. Surprisingly, the photodegradation performance for the recycled samples remained stable with negligible deactivation throughout the entire recyclability test. There is no significant loss of activity up to five catalytic cycles under the UV activation, which indicates that the as-prepared magnetic photocatalyst is stable and highly potential to be used as recyclable magnetic-photocatalyst for the removal of organic contaminants from water. Therefore, this nanocomposite would contribute for the advancement of the photocatalysis technology by offering a route

which is simple yet economic without the need in addressing challenges that associated complexed-separation process.

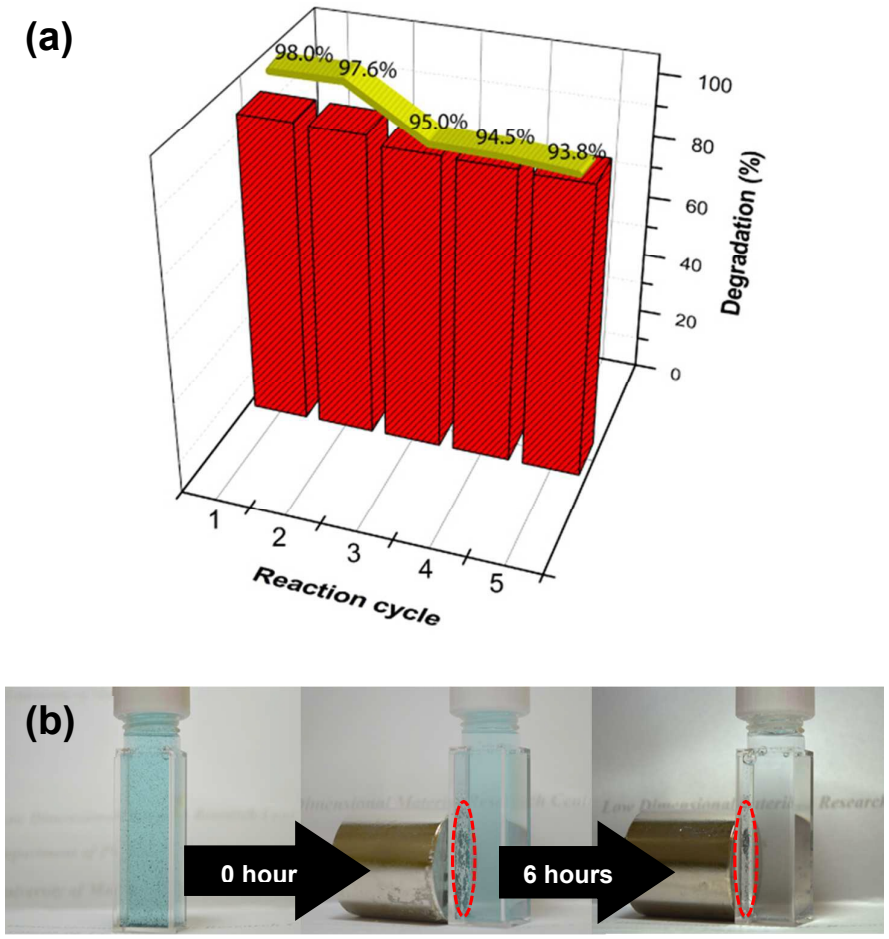

Fig. 13 (a) Recyclability of magnetic photocatalytic degradation of MB in the presence of $CoFe_2O_4$ decorated 3D TiO_2 magnetic nanocomposite. (b) Magnetic photocatalytic $CoFe_2O_4$-3D TiO_2 nanocomposites were recovered from the treated MB solution. The composite is set for magnetic separation after 6 consecutive hours of irradiation and could be reused several times without any significant loss of magnetic responsiveness and photocatalytic reactivity.

4. Conclusions

In summary, we have developed a highly $CoFe_2O_4$ decorated 3D urchin-like TiO_2 nanocomposite and test its feasibility to be used as magnetically recoverable photocatalyst. Detailed characterisations have been conducted to elucidate the morphologies, crystallinity and optical properties of the samples. The $CoFe_2O_4$ nanoparticles decorated 3D urchin-like TiO_2 nanocomposite show improved photocatalytic activity as well as excellent recyclability for possible sequential usage without significant loss of magnetic properties. Hence, it is perceived that current study could potentially serve as a potential route for the advancement of photocatalyst technology, especially for developing recyclable magnetic-nanophotocatalytic for wastewater treatment.

Acknowledgements

This project was supported by KPT-FRGS (FP038-2014B), e-Science fund (13-02-03-3093) and Postgraduate Research Grant (PPP) (PG027-2013B). Additional sources of funding from UMRG (RP007B-13AFR), High Impact Research Programme (UM.C/625/1/HIR/079) and HIR-MOHE (UM.C/625/1/HIR/MOHE/SC/06) are also highly appreciated.

References

1 K.T. Chung, G.E. Fulk and A.W. Andrews, *Appl. Environ. Microbiol.* 1981, **42**, 641–648.
2 B. Halling-Sørensen, S. Nors Nielsen, P. Lanzky, F. Ingerslev, H. Holten Lützhøft and S. Jørgensen, *Chemosphere*, 1998, **36**, 357–393.
3 H. Czili and A. Horvath, *Appl. Catal., B Environ.,* 2009, **89**, 342–348.
4 S. Devipriya and S. Yesodharan, *Sol. Energ. Mat. Sol. Cells*, 2005, **86**, 309–348.
5 J. Luo, J. H. Im, M. T. Mayer, M. Schreier, M. K. Nazeeruddin, N. G. Park, S. D. Tilley, H. J. Fan and M. Grätzel, Science, 2014, **345**, 1593.
6 C. Karunakaran and R. Dhanalakshmi, *Sol. Energ. Mat. Sol. Cells*, 2008, **92**, 588–593.
7 S. Girish Kumar, K. S. R. Koteswara Rao, *Nanoscale*, 2014, **6**, 11574-11632
8 D. O. Scanlon, C. W. Dunnill, J. Buckeridge, S. A. Shevlin, A. J. Logsdail, S. M. Woodley, C. R. A. Catlow, M. J. Powell, R. G. Palgrave, I. P. Parkin, G. W. Watson, T. W. Keal, P. Sherwood, A. Walsh and A. A. Sokol, *Nat Mater*, 2013, **12**, 798-801.

9 M. Biancardo, R. Argazzi and C.A. Bignozzi, *Inorg. Chem.*, 2005, **44** 9619–9621.

10 S. Wang, J.S. Lian, W.T. Zheng and Q. Jiang, *Appl. Surf. Sci.* 2012, **263**, 260–265.

11 O. Diwald, T. L. Thompson, T. Zubkov, Ed. G. Goralski, S. D. Walck and J. T. Yates, *J. Phys. Chem. B*, 2004, **108**, 6004–6008.

12 N. D. Abazović, L. Mirenghi, I. A. Janković, N. Bibić, D. V. Šojić, B. F. Abramović and M. I. Čomor, *Nanoscale Res. Lett.,* 2009, **4**, 518–525.

13. X. Zhang, L. Chen, H. Pan, Z.Q. Bao and X. F. Zhou, *Thin Solid Films*, 2014, **573**, 107–111.

13 Y. Rui, Y. Li, Q. Zhang and H. Wang, *CrystEngComm*, 2013, **15**, 1651-1656.

14 M. D. Roach, R. S. Williamson, I. P. Blakely and L. M. Didier, *Materials Science and Engineering: C*, 2016, **58**, 213-223.

15 H. Zhang and J.F. Banfield, *J. Mater. Chem.*, 1998, **8**, 2073–2076.

16 H. Zhang and J.F. Banfield, *J. Phy. Chem. B,* 2000, **104**, 3481–3487.

17 D. A. H. Hanaor and C. C. Sorrell, *J. Mater. Sci.* 2011, **46**, 855–874.

18 L. Xiang, X. Zhao, J. Yin and B. Fan, *J. Mater. Sci.,* 2012, **47**, 1436–1445.

19 G. Tian, Y. Chen, W. Zhou, K. Pan, C. Tian, X.-r. Huang and H. Fu, *CrystEngComm*, 2011, **13**, 2994-3000.

20 Y.J. Jiang, M.C. Li, D.D. Song, X.D. Li and Y. Yu, *J. Solid State Chem.*, 2014, **211**, 90–94.

21 J. Arbiol, J. Cerdà, G. Dezanneau, A. Cirera, F. Peiró, A. Cornet and J.R. Morante*, J. Appl. Phys*., 2002, **92**, 853–861.

22 R.J. Wang, X.H. Wang, X.G. Xi, R.B. Hu, G.H Jiang, *Adv. Mater. Sci. Eng.* 2012, 1–8.

23 J.Y. Chen, H.M. Zhang, P.R. Liu, Y. Wang, X.L. Liu, G.Y. Li, T.C. An and H.J. Zhao, *J. Colloid Interf. Sci.* 2014, **429**, 53–61.

24 K.K. Nanda, A. Maisels, F.E. Kruis, H. Fissan and S. Stappert, *Phys. Rev. Lett.* 2003, **91**, 106102.

25 R.Yogamalar, R. Srinivasan, A. Vinu, K. Ariga and A.C. Bose, *Solid State Comm.,* 2009, **149**, 1919–1923.

26 R. Sharma, B. Paul and P. Banerji, *Applied Surface Science*, 2010, **256**, 2232-2235.

27 X. Hou, X. Wang, B. Liu, Q. Wang, Z. Wang, D. Chen and G. Shen, *ChemElectroChem*, 2014, **1**, 108-115.

28 D.-Y. Jo and H. Yang, *Journal of Luminescence*, 2015, **166**, 227-232.

29 M. Ivanda, S. Musić, M. Gotić, A. Turković, A. M. Tonejc and O. Gamulin, *Journal of Molecular Structure*, 1999, **480–481**, 641-644.

30 H. L. Ma, J. Y. Yang, Y. Dai, Y. B. Zhang, B. Lu and G. H. Ma, *Applied Surface Science*, 2007, **253**, 7497-7500.

31 W. Su, J. Zhang, Z. Feng, T. Chen, P. Ying and C. Li, *The Journal of Physical Chemistry C*, 2008, **112**, 7710-7716.

32 Y. Zhang, C. X. Harris, P. Wallenmeyer, J. Murowchick and X. Chen, *The Journal of Physical Chemistry C*, 2013, **117**, 24015-24022.

33 G. Chen, *Journal of Alloys and Compounds*, 2015, **651**, 503-508.

34 J. H. Nicola, C. A. Brunharoto, M. Abramovich and C. E. T. Conçalves da Silva, *Journal of Raman Spectroscopy*, 1979, **8**, 32-34.

35 R.J. Betsch, H.L. Park, W.B. White, Mater, Res. Bull. 1991, **26**, 613.

36 T. Yu, Z. X. Shen, Y. Shi and J. Ding, *Journal of Physics: Condensed Matter*, 2002, **14**, L613.

37 S. Ayyappan, S. Mahadevan, P. Chandramohan, M. P. Srinivasan, J. Philip and B. Raj, *The Journal of Physical Chemistry C*, 2010, **114**, 6334-6341.

38 G. Shemer, E. Tirosh, T. Livneh and G. Markovich, *The Journal of Physical Chemistry C*, 2007, **111**, 14334-14338.

39 H. S. Kim, D. Kim, B. S. Kwak, G. B. Han, M.-H. Um and M. Kang, *Chemical Engineering Journal*, 2014, **243**, 272-279.

40 B.S. Holinsworth, D. Mazumdar, H. Sims, Q.C. Sun, M.K. Yurtisigi, S.K. Sarker, A. Gupta, W.H. Butler and J. L. Musfeldt, *Applied Physics Letters*, 2013, **103**, 082406.

41 A.V. Ravindra, P. Padhan and W. Prellier, *Applied Physics Letters*, 2012, **101**, 103505.

42 K. Dileep, B. Loukya, N. Pachauri, A. Gupta and R. Datta, *Journal of Applied Physics*, 2014, **116**, 103505.

43 L. Gan, S. M. Shang, C. W. M. Yuen, S. X. Jiang and E. L. Hu, *Applied Surface Science*, 2015, **351**, 140-147.

44 C. Leng, J. Wei, Z. Liu, R. Xiong, C. Pan and J. Shi, *J Nanopart Res*, 2013, **15**, 1-11.

45 D. Das and R. K. Dutta, *Journal of Colloid and Interface Science*, 2015, **457**, 339-344.

46 E. Kordouli, K. Bourikas, A. Lycourghiotis and C. Kordulis, *Catalysis Today*, 2015, **252**, 128-135.

47 S. Sood, S. Kumar, A. Umar, A. Kaur, S. K. Mehta and S. K. Kansal, *Journal of Alloys and Compounds*, 2015, **650**, 193-198.

48 J. Tian, Y. Leng, H. Cui and H. Liu, *Journal of Hazardous Materials*, 2015, **299**, 165-173.

49 W.S. Chiu, P.S. Khiew, M. Cloke, D. Isa, T.K. Tan, S. Radiman, R. Abd-Shukor, M.A. Abd. Hamid, N.M. Huang, H.N. Lim and C.H. Chia, *Chem. Eng. J.*, 2010, **158**, 345–352.

50 P. Sathishkumar, N. Pugazhenthiran, R. V. Mangalaraja, A. M. Asiri and S. Anandan, *Journal of Hazardous Materials*, 2013, **252–253**, 171-179.

51 P. Xiong, J. Zhu and X. Wang, *Industrial & Engineering Chemistry Research*, 2013, **52**, 17126-17133.

52 Y. Li, J. Niu, L. Yin, W. Wang, Y. Bao, J. Chen and Y. Duan, *Journal of Environmental Sciences*, 2011, **23**, 1911-1918.

53 B. Abramović, V. Despotović, D. Šojić and N. Finčur, *Reac Kinet Mech Cat*, 2015, **115**, 67-79.

Conflict of Interests

The author(s) declare(s) that there is no conflict of interests regarding the publication of this study.

Design of New Magnetic-Photocatalyst Nanocomposites ($CoFe_2O_4$-TiO_2) as Smart Nanomaterials for Recyclable-Photocatalysis Application

Graphical Abstract

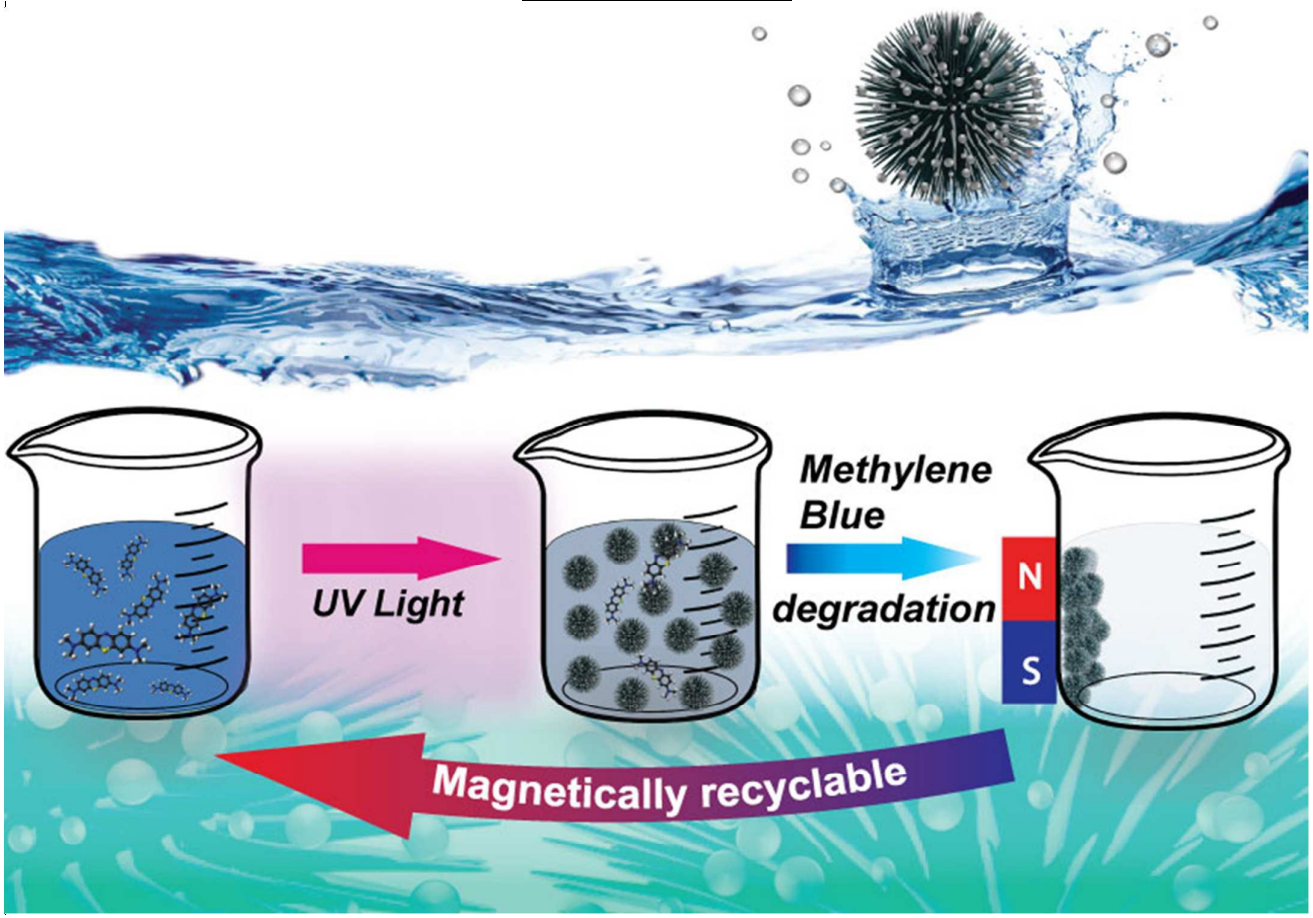

Magnetically recyclable 3D $CoFe_2O_4$-TiO_2 Photocatalyst Nanocomposite